

# Polarisation of the Broad $H\alpha$ Wing in Symbiotic Stars

Jerry Jaiyul Yoo<sup>1</sup>  $\star$ , Jih-Yong Bak<sup>2</sup> and Hee-Won Lee<sup>3</sup>

<sup>1</sup> *Astronomy Program, School of Earth and Environmental Sciences, Seoul National University, Seoul 151-742, Korea.*

<sup>2</sup> *Department of Astronomy, Yonsei University, 134 Shinchon, Seodaemunku, Seoul 120-749, Korea*

<sup>3</sup> *Department of Geoinformation Sciences, Sejong University, Seoul 143-747, Korea*

2 December 2024

## ABSTRACT

In many symbiotic stars there appear broad wings around  $H\alpha$ , of which the formation mechanism proposed thus far includes a fast outflow, the inner accretion disc motion, electron scattering and Raman scattering of  $Ly\beta$ . We adopt a Monte Carlo technique to simulate the Raman scattering of UV photons that are converted into optical photons around  $H\alpha$  forming broad wings, and compute its polarisation. Noting that many symbiotic stars exhibit a bipolar nebular morphology and polarisation flip in the red wing part of the Raman scattered  $O\ vI$  features, we assume that the neutral scattering region is composed of the two components. The first component is a static cylindrical shell with finite thickness and the other component is a finite slab that is moving away with velocity  $v_p = 100\text{ km s}^{-1}$  along the symmetry axis of the first component. The cylindrical shell component yields polarisation in the direction parallel to the cylinder axis. The strongest polarisation is obtained in the limit where the height of the cylinder approaches zero and the scattering region effectively becomes a circular ring. As the height of the cylinder increases, the resultant polarisation decreases and becomes negligible in the limit of the infinite cylinder. The polarisation near the line-centre is weaker than in the far wing regions because of the large Rayleigh scattering numbers due to the large scattering cross sections near the line centre. The receding polar scattering component produces strong polarisation in the direction perpendicular to the cylinder axis. In the presence of a  $Ly\beta$  emission line part with an equivalent width  $\sim 0.5\text{ \AA}$ , the polarised flux exhibits a local maxima at  $\lambda = 6578\text{ \AA}$  that corresponds to the receding velocity with  $6.4v_p$  relative to  $H\alpha$ . When the both scattering components coexist, the polarisation is characterised by weak parallel polarisation near the line-centre and strong perpendicular polarisation in the red part. We discuss the observational implications of our computation.

**Key words:** line: formation — line: profiles — polarisation — radiative transfer — scattering — binaries: symbiotic

## 1 INTRODUCTION

Symbiotic stars are generally known to be interacting binaries of a mass losing giant and a hot white dwarf surrounded by an ionised nebula that is responsible for various prominent emission lines (Kenyon 1986). In the spectra of symbiotic stars, there exist very unique emission features around  $6830\text{ \AA}$  and  $7088\text{ \AA}$ . Schmid (1989) proposed that they are formed via Raman scattering by atomic hydrogen of  $O\ vI$  1032, 1038 doublet. When an  $O\ vI$  line photon that is more energetic than  $Ly\alpha$  is incident upon a hydrogen atom in its ground  $1s$  state, it subsequently re-emits an outgoing photon with de-excitation into either  $1s$  state or  $2s$  state. In the first case, a Rayleigh scattering process happens with no change in the frequency in the scatterer's rest frame. The second case corresponds to a Raman scattering process, from which we obtain a  $6830$  line photon from an incident  $O\ vI$  1032 photon and a  $7088$  line photon from an incident  $O\ vI$  1038 photon.

$\star$  E-mail: jyyu@astro.snu.ac.kr

The scattering cross sections associated with these Raman processes are of order  $\sigma \sim 10^{-23} \text{ cm}^2$  (e.g. Schmid 1989; Nussbaumer, Schmid & Vogel 1989; Sadeghpour & Dalgarno 1992; Lee & Lee 1997), and therefore the operation of the O VI Raman scattering requires the existence of both a highly ionized O VI emission region and a fairly extensive neutral scattering region with H I column density  $N_{HI} \sim 10^{23} \text{ cm}^{-2}$ . The scattering cross section is very sensitive to the wavelength of the incident radiation in such a way that it steeply increases as the wavelength approaches the resonance wavelength of the scatterer. Therefore, continuum photons with wavelength near that of the Ly $\beta$  will be scattered in a neutral hydrogen region with much lower H I column density than that is required for O VI Raman scattering.

van Winckel, Duerbeck & Schwarz (1993) showed that most symbiotic stars in the southern hemisphere exhibit very broad wings around H $\alpha$ . A similar result was reported for those in the northern hemisphere by Ivison, Bode & Meaburn (1994). The full width at zero intensity often exceeds  $2000 \text{ km s}^{-1}$ . Similar broad wings also appear in young planetary nebulae, including M2-9, Mz3, and IC 4997 (e.g. Arrieta & Torres-Peimbert 2002; Miranda, Torrelles & Eiroa 1996). In particular, for M2-9, Balick (1989) reported the existence of very broad H $\alpha$  wings with a width  $\sim 10^4 \text{ km s}^{-1}$ . Remarkably enough, Selvelli & Bonifacio (2000) presented the VLT spectrum of the symbiotic star RR Tel which shows H $\alpha$  wings extending up to  $12000 \text{ km s}^{-1}$ . According to van de Steene, Wood & van Hoof (2000), post AGB stars also exhibit broad H $\alpha$  wings.

There have been many theoretical suggestions for the broad H $\alpha$  wings formation mechanism. These include fast outflows (e.g. Schmutz et al. 1994), electron scattering (e.g. Bernat & Lambert 1978), the accretion disc (e.g. Quiroga et al. 2002) and the Raman scattering of Ly $\beta$ . In this paper, we will not consider all those theoretical models but will focus only on the H $\alpha$  wing formation via the Raman scattering of Ly $\beta$ .

Nussbaumer et al. (1989) discussed the astrophysical importance of the Raman scattering by atomic hydrogen and proposed that broad H $\alpha$  wings can be formed through the Raman scattering of Ly $\beta$ . This idea has been applied to a young and compact planetary nebula IC 4997 by Lee & Hyung (2000). They computed the wing profile formed through Raman scattering of flat continuum around Ly $\beta$  and obtained an excellent agreement with the observed profile. A similar success has been achieved for many symbiotic stars by Lee (2000).

The existence of a thick H I region in symbiotic stars and young planetary nebulae can also be inferred from the He II Raman scattered features. Because He II is also a single electron atom, the wavelengths associated with the transitions from  $n = 2m$  state to the  $2s$  state are very close to those corresponding to the  $m$ -th Lyman series of hydrogen. Therefore, He II Raman scattering requires much less H I column density  $N_{HI} \sim 10^{20} \text{ cm}^{-2}$  than O VI 1032, 1038 doublet. The He II Raman scattered lines have been found in the spectra of RR Tel and He 2-106 (e.g. van Groningen 1993; Lee, Kang & Byun 2001) and young planetary nebulae M2-9 (Lee et al. 2001), which highlights the plausibility of the operation of the Ly $\beta$  Raman scattering in these objects. Therefore, in this work, we will consider Raman scattering of Ly $\beta$  in neutral regions with  $N_{HI} = 10^{20} - 10^{23} \text{ cm}^{-2}$ .

Spectropolarimetry will provide valuable information on the H $\alpha$  wing formation mechanism. Raman scattered radiation consists of purely scattered radiation without any mixing of direct radiation, and therefore Raman scattered radiation can be strongly polarised. Polarisation is also dependent on the scattering geometry. Spectropolarimetry may reveal the circumstellar matter distribution and be useful to understand the mass loss process of the giant component.

In this paper, we will compute the profile and the polarisation of H $\alpha$  wings that are assumed to be formed through Raman scattering of Ly $\beta$ . In section 2, we will briefly introduce the basic atomic physics relevant to the H $\alpha$  wing formation and describe the Monte Carlo procedure. In section 3, we present our main results. In the final section we discuss our results and observational implications.

## 2 H $\alpha$ WING FORMATION THROUGH RAMAN SCATTERING

### 2.1 Branching Ratio

A Ly $\beta$  photon incident on a scattering region consisting of atomic hydrogen undergoes either Rayleigh scattering or Raman scattering. In particular, in the latter case the scattering H atom de-excites to the  $2s$  state resulting in an outgoing H $\alpha$  photon. Due to the scattering incoherency, if an incident photon near the Ly $\beta$  line centre is Raman-scattered, then the outgoing photon finds itself in the H $\alpha$  wing region much further from the line centre by a factor of 6.4 than from that of Ly $\beta$  line centre (e.g. Schmid 1989, Nussbaumer et al. 1989). Lee & Hyung (1999) emphasised that the profile of H $\alpha$  wings formed by Raman scattering of Ly $\beta$  will be proportional to  $\Delta\lambda^{-2}$ , when the Raman scattering optical depth is small. However, the detailed conversion process from a UV photon into an optical photon is dependent on the branching ratio of the Rayleigh scattering and Raman scattering cross sections (e.g. Schmid 1996). In this subsection, we illustrate a basic calculation that provides an approximate branching ratio near the Ly $\beta$  line-centre.

The branching ratio of the Rayleigh process to the Raman process is well known in the literature, which is around 1:7. However, this ratio is dependent on the wavelength of the incident photon.

The differential cross section for Rayleigh scattering is given by

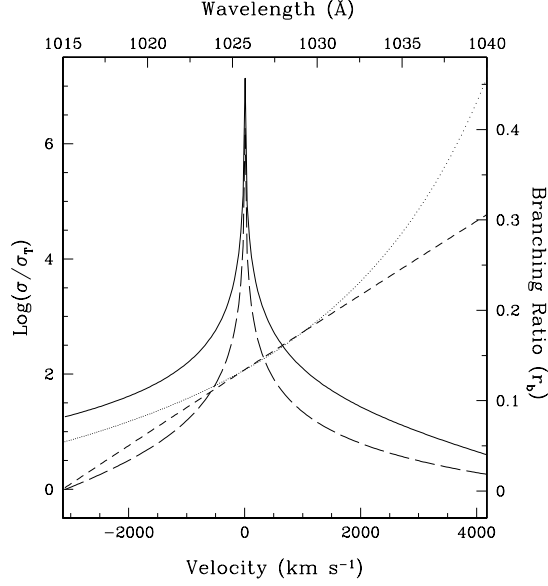


**Figure 1.** Branching ratio of the Rayleigh scattering to the Raman scattering. The solid and the long dashed lines represent the differential cross sections of Rayleigh and Raman scatterings in units of Thomson scattering cross section, respectively. The branching ratio of the Rayleigh scattering to the Raman scattering and its first order approximation are shown in the dotted and the short dashed lines, respectively.

$$\left(\frac{d\sigma}{d\Omega}\right)_{Ray} = r_0^2 \left| \frac{1}{m\hbar} \sum_I \left( \frac{\omega(\mathbf{p} \cdot \boldsymbol{\epsilon}^{\alpha'})_{AI}(\mathbf{p} \cdot \boldsymbol{\epsilon}^{\alpha})_{IA}}{\omega_{IA}(\omega_{IA} - \omega)} - \frac{\omega(\mathbf{p} \cdot \boldsymbol{\epsilon}^{\alpha})_{AI}(\mathbf{p} \cdot \boldsymbol{\epsilon}^{\alpha'})_{IA}}{\omega_{IA}(\omega_{IA} + \omega)} \right) \right|^2, \quad (1)$$

and the Raman scattering differential cross section is

$$\left(\frac{d\sigma}{d\Omega}\right)_{Ram} = r_0^2 \left(\frac{\omega'}{\omega}\right) \left| \frac{1}{m\hbar} \sum_I \left( \frac{(\mathbf{p} \cdot \boldsymbol{\epsilon}^{\alpha'})_{BI}(\mathbf{p} \cdot \boldsymbol{\epsilon}^{\alpha})_{IA}}{\omega_{IA} - \omega} + \frac{(\mathbf{p} \cdot \boldsymbol{\epsilon}^{\alpha})_{BI}(\mathbf{p} \cdot \boldsymbol{\epsilon}^{\alpha'})_{IA}}{\omega_{IA} + \omega'} \right) \right|^2, \quad (2)$$

where the subscript  $A$  stands for the initial quantum state of the scatterer,  $I$  for the intermediate state and  $B$  for the final state. We have  $A = 1s, B = 2s$  for the Raman process and  $A = B = 1s$  for the Rayleigh process (Sakurai 1967). Here,  $\omega_{IA} = \hbar^{-1}(E_I - E_A)$  is the angular frequency for the transition between the initial state  $A$  and the intermediate state  $I$ ,  $r_0$  is the classical electron radius, and  $\boldsymbol{\epsilon}^{\alpha}$  represents the polarisation vector of the incident photon. The primed quantities correspond to those associated with the outgoing photon. In particular, the energy conservation relation for the Raman scattering case gives

$$\omega' = \omega - \omega_{\alpha}, \quad (3)$$

where  $\omega_{\alpha}$  represents the angular frequency of the Ly $\alpha$  transition. We are interested only in scatterings occurring in the wing regime far from the resonance and therefore omit the damping term in the denominator of each transition matrix element.

For an incident photon around Ly $\beta$ ,  $\omega \simeq \omega_{\beta}$  and the cross sections for both scattering processes are dominantly contributed by the first term in the summation corresponding to  $I = 3p$  in Eqs. 1 and 2. Since the angular distribution of the scattered radiation is the same for both processes, we can write the branching ratio  $r_b$  of the cross sections for Rayleigh scattering and Raman scattering by

$$r_b(\omega) = \left(\frac{\omega'}{\omega}\right) \left| \frac{A_1/\Delta\omega - A_2}{A_3/\Delta\omega - A_4} \right|^2 \simeq \left(\frac{\omega_{\beta} - \omega_{\alpha}}{\omega_{\beta}}\right) \left(\frac{A_1}{\omega_{\beta}A_3}\right)^2 \left[ 1 + \left(\frac{\omega_{\beta}}{\omega_{\beta} - \omega_{\alpha}} - 3 + \frac{2\omega_{\beta}A_2}{A_1} - \frac{2\omega_{\beta}A_4}{A_3}\right) \frac{\Delta\omega}{\omega_{\beta}} \right], \quad (4)$$

where we set  $\omega = \omega_{\beta} + \Delta\omega$ ,  $|\Delta\omega| \ll \omega_{\beta}$ .

The matrix elements that appear in Eq. 4 are explicitly given by

$$\begin{aligned} A_1 &= \langle 2s \parallel p \parallel 3p \rangle \langle 3p \parallel p \parallel 1s \rangle, \\ A_2 &= \sum_{I \neq 3p} \frac{\langle 2s \parallel p \parallel I \rangle \langle I \parallel p \parallel 1s \rangle}{\omega_{I1} - \omega_{\beta} - \Delta\omega} + \sum_{I \neq 3p} \frac{\langle 2s \parallel p \parallel I \rangle \langle I \parallel p \parallel 1s \rangle}{\omega_{I1} + (\omega_{\beta} - \omega_{\alpha} + \Delta\omega)}, \\ A_3 &= \frac{|\langle 3p \parallel p \parallel 1s \rangle|^2}{\omega_{\beta}}, \end{aligned}$$

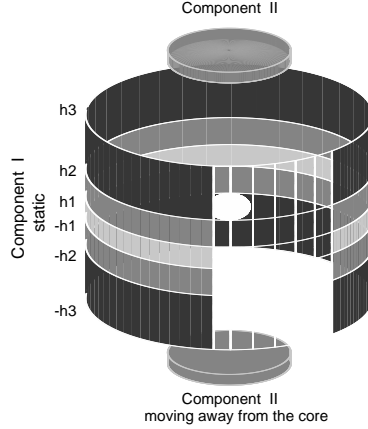


**Figure 2.** Schematic view of the scattering geometry. The central core represents the emission region. The static cylindrical shell denoted by Component I is composed of three layers stratified from the equatorial region. The layers are characterised by different H I densities and heights  $h_1, h_2, h_3$ . The circular slabs (Component II) with homogeneous H I density are located in the polar direction, moving away from the core.

$$A_4 = \sum_{I \neq 3p} \frac{|\langle I \| p \| 1s \rangle|^2}{\omega_{I1}(\omega_{I1} - \omega_\beta - \Delta\omega)} - \sum_{I \neq 3p} \frac{|\langle I \| p \| 1s \rangle|^2}{\omega_{I1}(\omega_{I1} + \omega_\beta + \Delta\omega)}. \quad (5)$$

It is noted that the summation extends to the continuum states, where the sum over all continuum states should be written in an integral form.

The explicit representations of the matrix elements are found in the literature (e.g. Berestetskii, Lifshitz & Pitaevskii 1971; Saslow & Mills 1969; Karzas & Latter 1961) and a straightforward numerical computation gives  $A_1/(\omega_\beta A_3) = 0.9268$ ,  $\omega_\beta A_4/A_3 = 17.91$ ,  $\omega_\beta A_2/A_1 = -30.37$ . These results are directly substituted into Eq. 4 to yield

$$r_b(\omega) \simeq 0.1342 - 12.50\Delta\omega/\omega_\beta. \quad (6)$$

In Fig. 1 we present the branching ratio of the Raman scattering cross section to the Rayleigh cross section. The short dashed line represents the approximate result given in Eq. 6, whereas the dotted line stands for the result obtained by using the whole Kramers-Heisenberg relation. The approximate relation gives the error less than 10 per cent in the range  $\Delta V \leq 1000 \text{ km s}^{-1}$ . This implies that the contribution from other  $np$  states is not negligible. From Fig. 1 we see that the branching ratio varies in a rather large range from 0.05 to 0.45 in the wavelength interval from 1015 Å to 1040 Å. Since the broad feature around 7088 Å that is Raman-scattered O VI 1038 is often found in the spectra of symbiotic stars, it is necessary to investigate the Raman conversion efficiency for a broad range of the branching ratios.

## 2.2 Scattering Geometry

In our calculations we assume that the neutral scatterers are simply distributed in a cylindrical shell. Fig. 2 shows a schematic view of the scattering geometry. Many symbiotic stars exhibit a bipolar nebular morphology, which is characterised by the accumulation of circumstellar materials near the equatorial plane. However, with the lack of detailed and quantitative models of the circumstellar region, we just assume that the neutral hydrogen component forms a finite cylindrical shell (Component I in Fig. 2) with the center coinciding with the Ly $\beta$  emission source. The cylindrical shell is assumed to be of constant H I density and hence characterised by the radius  $r$  and the height  $h$ .

In the spectropolarimetric data presented by Harries & Howarth (1996), the Raman scattered O VI 6830 and 7088 features exhibit polarisation flip in the red wing part. Schmid (1996) interpreted the polarisation flip in the red wing part by scattering in the slow stellar wind from the giant component. Another interpretation has been proposed by Lee & Park (1999), who assumed the existence of an accretion disc around the white dwarf component via gravitational capture of the slow stellar wind around the giant component. According to their model, the emission region is formed around the accretion disc, and the main double peaks shown in the Raman scattered features are attributed to the disc motion viewed in the equatorial direction, where the main scattering region is formed around the giant component. In order to explain the polarisation flip in the red wing part, there has to be another scattering component that is moving away from the emission region in the direction perpendicular to the equatorial plane.

In this work, we will also consider that H $\alpha$  wings are significantly contributed by this polar scattering region (Component II in Fig. 2). It is uncertain whether this polar scattering component is ubiquitous in all symbiotic stars. Harries & Howarth (1996) showed that a significant fraction of symbiotic stars may possess this component, under the picture presented by Lee

& Park (1999). Because the polar component is assumed to be receding from the emission region, it will mainly affect the red part of the H $\alpha$  wings.

With this geometry, we prepare a photon source at the centre, from which the UV photons around Ly $\beta$  are injected into the scattering region. For a given incident photon the corresponding cross-sections of the Rayleigh and the Raman scatterings are calculated from the Kramers-Heisenberg formula (e.g., Sakurai 1967; Bethe & Salpeter 1957). The ratio of the two cross-sections is dependent only upon the incident wavelength (Lee & Lee 1997). According to this ratio, we decide whether a given scattering event is Rayleigh or Raman in the Monte Carlo procedure.

Although the UV photons may be Rayleigh scattered several times, the scattering regions are assumed to be transparent to the optical photons converted by Raman scattering. Therefore, an incident UV photon suffers a number of Rayleigh scatterings until it is Raman scattered or escapes the scattering region as a UV photon.

We typically inject  $10^5$  UV photons in a bin with  $\Delta\lambda = 0.005$  Å around Ly $\beta$ , and calculate the polarisation state at each scattering. Finally we collect Raman scattered photons according to the emergent direction cosine of the wave vector with a bin size of  $\Delta\mu = 0.1$ .

### 2.3 Computation of Polarisation

Because our scattering geometry is azimuthally symmetric, under the assumption that the emission source is not circularly polarised, no circular polarisation will develop. Hence we only consider linear polarisation that may develop either in parallel or perpendicular to the symmetry axis. We will distinguish the polarisation direction by the sign of the polarisation. That is, we will denote the polarisation perpendicular to the symmetry axis by positive polarisation and parallel polarisation by negative polarisation.

In the case of single electron atoms including hydrogen, the fine structure level splitting is so small due to accidental degeneracy. Therefore, any off-resonance scattering is characterised by the same scattering phase function as that of the Thomson scattering, which was shown by Stenflo (1980). Since the H $\alpha$  wings spread over  $\geq 1000$  km s $^{-1}$ , resonance scattering contributes very little to the wing formation. Hence, in this work, the relevant scattering phase function is that for Thomson scattering.

In the computation of linear polarisation, we adopt the density matrix formalism, in which the polarisation state is described by a  $2 \times 2$  Hermitian matrix  $\rho$ . In particular, with respect to the symmetry axis that is taken as the  $z$ -axis in the usual spherical coordinate, we choose the polarisation basis vectors by  $\epsilon_1 = (\sin \phi, -\cos \phi, 0)$ ,  $\epsilon_2 = (\cos \theta \cos \phi, \cos \theta \sin \phi, \sin \theta)$  for a given line photon with wavevector  $\hat{\mathbf{k}} = (\sin \theta \cos \phi, \sin \theta \sin \phi, \cos \theta)$ , the linear polarisation  $p$  is obtained from the difference of the main diagonal elements of the density matrix  $\rho$ ,

$$p = \rho_{11} - \rho_{22}. \quad (7)$$

The relation between the density matrix  $\rho'$  of the scattered radiation with wavevector  $\hat{\mathbf{k}}' = (\sin \theta' \cos \phi', \sin \theta' \sin \phi', \cos \theta')$  and  $\rho$  of the incident radiation is given by

$$\begin{aligned} \rho'_{11} &= \rho_{11} \cos^2 \Delta\phi - \rho_{12} \cos \theta \sin 2\Delta\phi + \rho_{22} \cos^2 \theta \sin^2 \Delta\phi, \\ \rho'_{12} &= \frac{1}{2} \rho_{11} \cos \theta' \sin 2\Delta\phi + \rho_{12} (\cos \theta \cos \theta' \cos 2\Delta\phi + \sin \theta \sin \theta' \cos \Delta\phi) - \rho_{22} \cos \theta (\sin \theta \sin \theta' \sin \Delta\phi + \frac{1}{2} \cos \theta \cos \theta' \sin 2\Delta\phi), \\ \rho'_{22} &= \rho_{11} \cos^2 \theta' \sin^2 \Delta\phi + \rho_{12} \cos \theta' (2 \sin \theta \sin \theta' \sin \Delta\phi + \cos \theta \cos \theta' \sin 2\Delta\phi) + \rho_{22} (\cos \theta \cos \theta' \cos \Delta\phi + \sin \theta \sin \theta')^2, \end{aligned} \quad (8)$$

where  $\Delta\phi = \phi' - \phi$ .

It can be also shown that the angular distribution of the scattered radiation for an incident photon with  $\hat{\mathbf{k}}$  and  $\rho$  is given by the trace of  $\rho'(\theta', \phi', \theta, \phi)$  (e.g. Lee, Blandford & Western 1994). Therefore, once the wavevector  $\hat{\mathbf{k}}'$  of a scattered photon is chosen from  $\rho'$ , the polarisation is also determined at the same time. It is also noted that the density matrix is normalised each time so that it has a unit trace.

## 3 RESULTS

First, we present two idealised cases in order to obtain a qualitative understanding of the polarisation development through Raman scattering. Next, assuming the simple geometry we calculate the profile and the polarisation for various geometrical parameters. Then we present two applications for more realistic geometries.

### 3.1 Infinite Slab

To investigate the dependence of the polarisation on the number of Rayleigh scattering that a photon suffers, we just focus on the scattering events, ignoring other effects. An incident photon can escape and be counted only if it attains the prescribed number of scattering.

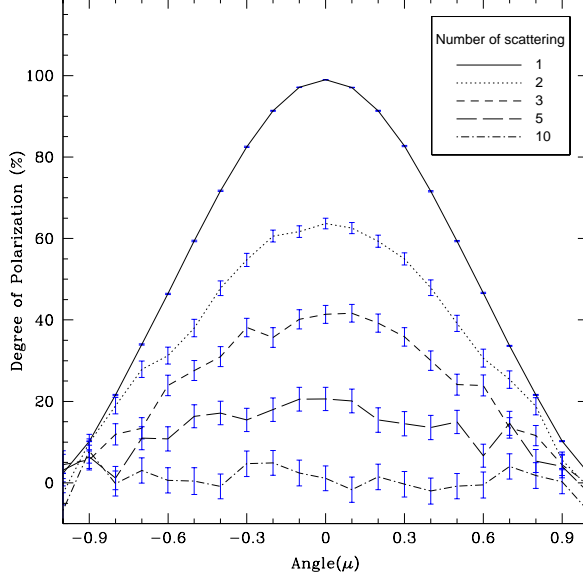


**Figure 3.** Polarisation of the Raman scattered photons for various lines of sight. UV photons are normally incident on the plane. Various types of lines represent the number of scatterings that the outgoing photon suffers. The polarisation is set to be positive when the polarisation direction is perpendicular to the symmetry axis. The error bars represent  $1\text{-}\sigma$ .

We typically inject  $10^4$  photons. In Fig. 3, the polarisation steeply decreases as the scattering number increases. If a photon is scattered three times, its maximal polarisation reduces to about 40%, and almost zero polarisation is observed when the scattering number exceeds ten.

Next, we present an idealised case of the normal incidence to the infinite slab in Fig. 4. We also inject  $10^4$  UV photons in a bin with  $\Delta\lambda = 0.05 \text{ \AA}$  with a full width  $6 \text{ \AA}$  centred at  $\text{Ly}\beta$ . They are normally incident to the infinite slab lying in the  $x - y$  plane. The  $\text{H I}$  column density is set to be  $5 \times 10^{20} \text{ cm}^{-2}$ .

Despite the large column density, for an incident UV photon far from the resonance wavelength of  $\text{Ly}\beta$ , the scattering region is optically thin and hence the Raman conversion rate is very low. However, radiation in this region is highly polarised because most photons suffer few scatterings, for which single scattering limit is achieved.

As the wavelength goes close to the  $\text{Ly}\beta$  line centre, the cross-section increases steeply. Most incident UV photons suffer a few Rayleigh scatterings. They escape from the slab by the final Raman scattering and contribute to the broad  $\text{H}\alpha$  wing formation. The flux near the  $\text{Ly}\beta$  line centre is typically polarised by about 40% in the equatorial direction, which is weaker than in the far wing regions. The weakening of polarisation in this region is attributed to the increased Rayleigh scattering numbers before escape by Raman scattering.

### 3.2 Polarisation for Various Heights of the Cylindrical Scattering Regions

We assume that the  $\text{H I}$  number density is constant throughout the scattering region of Component I in Fig. 2 ( $h \equiv h_1 = h_2 = h_3$ ), and obtain the profile and polarisation of broad  $\text{H}\alpha$  wings changing the ratios  $h/r$  of height to radius. In this work, just for simplicity and with lack of detailed information of the circumstellar matter distribution, we assume that the thickness of the  $\text{H I}$  cylindrical shell is much smaller than the radius. The profiles and polarisation of the broad  $\text{H}\alpha$  wings for various lines of sight are shown for several ratios in Figs. 5 and 6.

The radiation emergent in the polar direction is almost unpolarised because of the symmetry, which provides a check of our code. When the observer is in the equatorial direction, the Raman scattered radiation exhibits negative polarisation. As the height to radius ratio approaches zero, the scattering region is regarded as a circular ring, which yields the strongest polarisation 33% in the direction parallel to the symmetry axis of the circular ring. Since photons falling on to far wing regions are scattered fewer times than those contributing to near wing regions, the polarisation in far wing regions is much stronger than that near the  $\text{H}\alpha$  centre. Therefore, it is particularly notable that the Raman scattering wings are characterised by weak polarisation near the centre and strong polarisation at far wing regions, in the direction of the symmetry axis.

As the height increases relative to the radius, for a given line of sight, there can be a broad range of scattering angles. Therefore a superposition of electric vectors associated with the scattered radiation lessens the overall polarisation. In Fig. 6, it is apparent that the polarisation weakens as  $h/r$  increases. When  $h/r = 2$ , we obtain  $\text{H}\alpha$  wings polarised up to 10 per cent observed from the equatorial direction, which is much smaller than 30 per cent obtained in the case of  $h/r = 0.5$ .

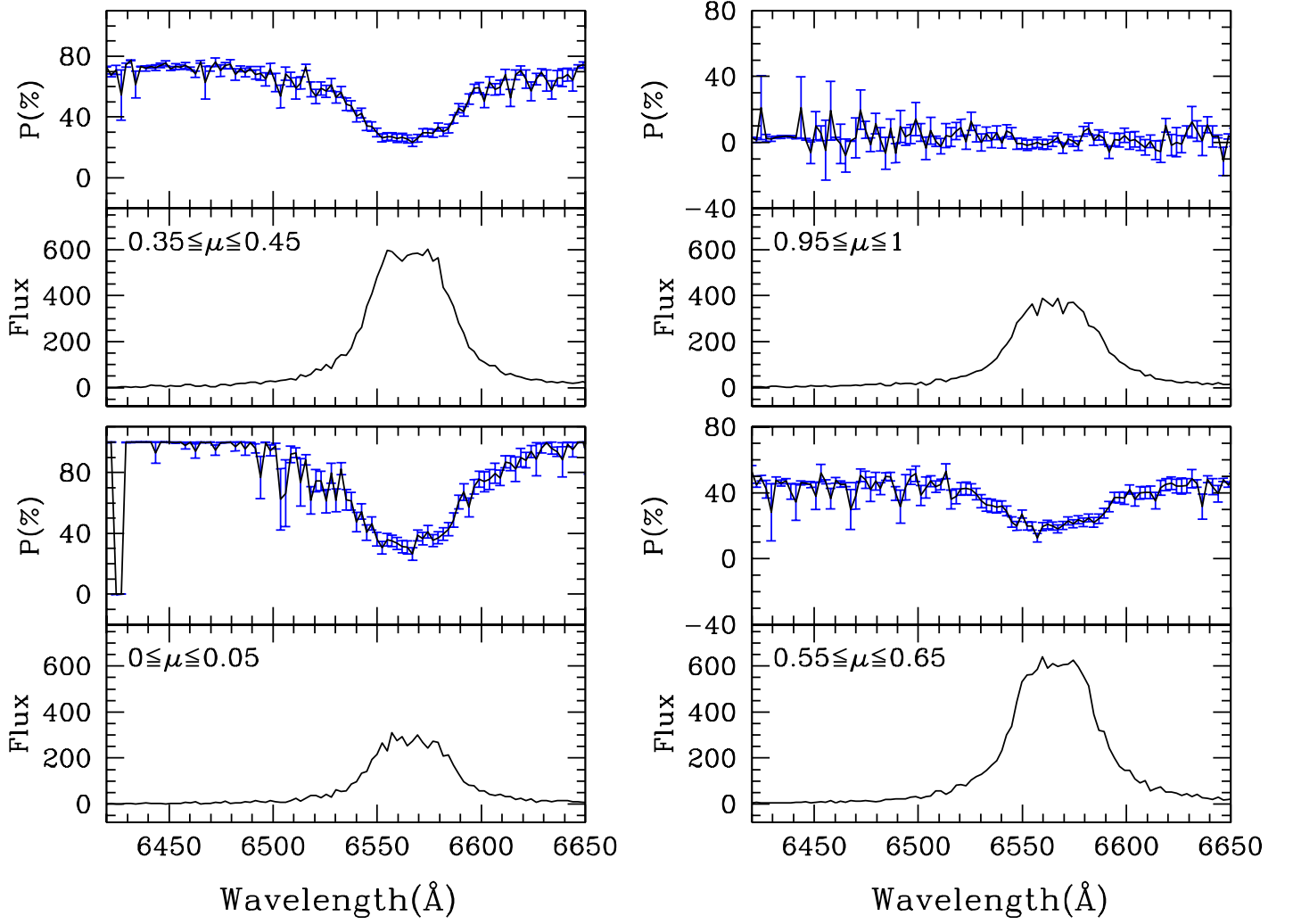


**Figure 4.** Profiles and polarisation of Raman scattered photons for various lines of sight.  $10^4$  UV photons are injected normally onto the infinite slab. The H I column density is set to be  $5 \times 10^{20} \text{cm}^{-2}$ . The error bars represent  $1-\sigma$ .

This trend will continue until the geometry is approximately regarded as an infinite cylinder. In this case, when the cylinder has enough thickness, emergent Raman scattered wings will be contributed to equally from all directions of incidence, and will be completely unpolarised. We increase the ratio  $h/r$  to as high as 5, which corresponds to the case that UV radiation from the emission source with  $\theta > 10^\circ$  will be incident on to the scattering region. As is shown in upper panels of Figs. 5 and 6, we obtain negligible polarisation in this case for all lines of sight.

However, we also see the weakly polarised parts in far blue and red regions for the case  $h/r = 5$ . This polarisation developed in the direction perpendicular to the symmetry axis is attributed to the limb effect. That is, the cylindrical shell is optically thin in the direction normal to the shell for far blue or red wing photons. Therefore, only a small fraction  $\tau_w$  of photons incident in this direction will be scattered, where  $\tau_w$  is the Raman scattering optical depth in this direction. However, when the incident photon has the wavevector  $\hat{k}$  with  $\hat{k} \cdot \hat{z} = \mu \simeq 1$ , the fraction of scattered photons increases to  $\tau_w / \sqrt{1 - \mu^2}$  which is much larger than  $\tau_w$ . This limb effect strengthens the positive polarisation component and results in polarisation in the perpendicular to the symmetry axis.

In the cylinder scattering model, we may summarise that the polarisation develops in the direction parallel to the symmetry axis, and that the polarisation is weaker near the H $\alpha$  centre due to a large Rayleigh scattering number than it is in the far wing regions.

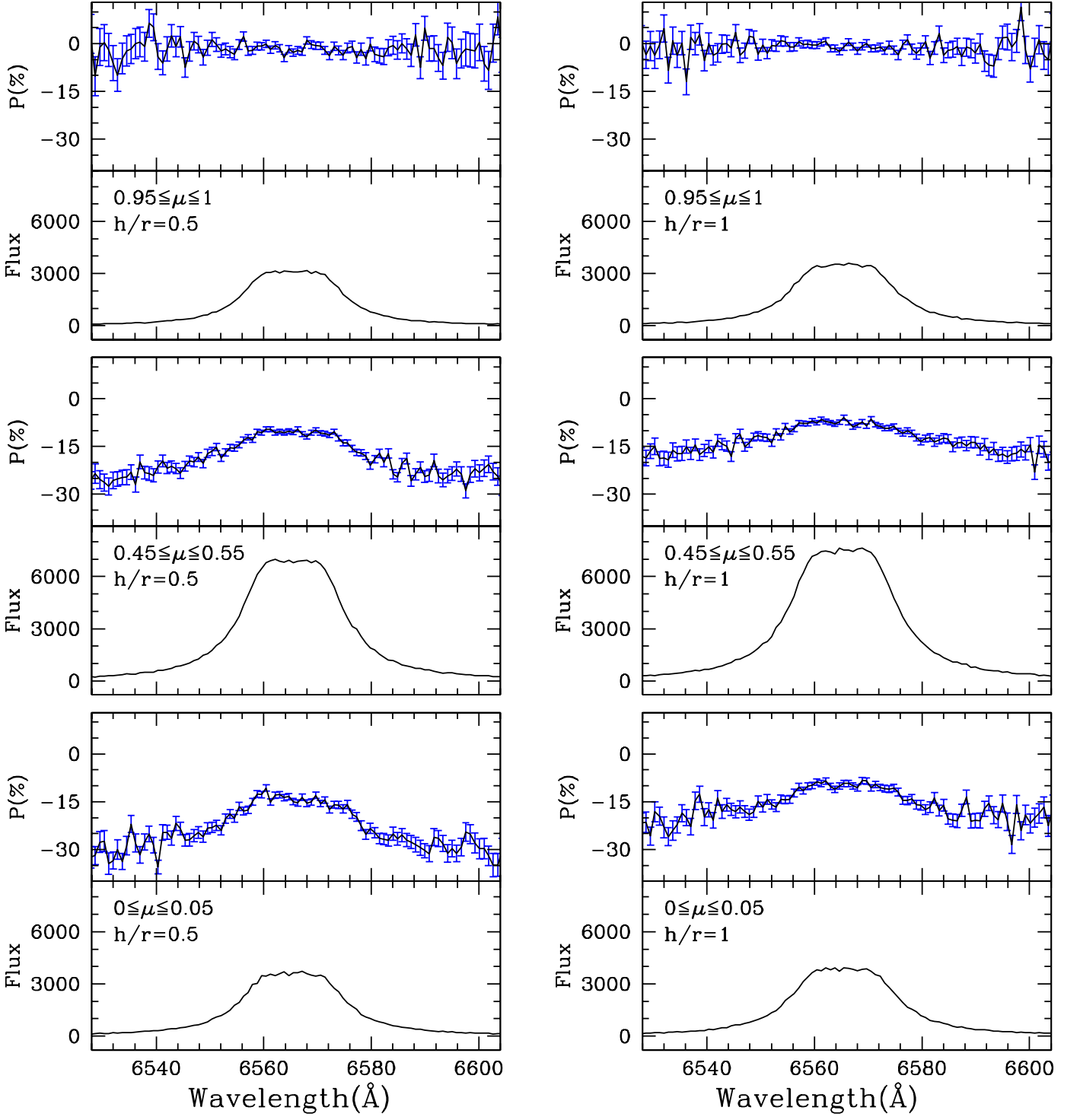


**Figure 5.** Profiles and polarisation of broad H $\alpha$  wings for various lines of sight. Here we consider only Component I in Fig. 2 with  $h \equiv h_1 = h_2 = h_3$ . The height to radius ratios  $h/r$  of the H I cylindrical shell are 0.5 and 1 for left and right panels, respectively.  $10^5$  UV photons in a bin with  $\Delta\lambda = 0.005$  Å are injected to the H I component I. The homogeneous H I column density is set to be  $10^{20}\text{cm}^{-2}$ . The error bars represent  $1\text{-}\sigma$ .

### 3.3 Hybrid Model of Cylindrical Shells

We present a hybrid model of Component I in Fig 2 consisting of three stratified layers ( $h_1 < h_2 < h_3$ ) with different H I column densities. In this model, the density is highest in the equatorial region and decreases as the latitude increases. This may mimic the matter distribution in the circumstellar region more realistically. This hybrid model can be viewed as a linear superposition which is the solid angle weighted sum of the previous models with various ratios and homogeneous hydrogen number density.

We consider two different cases denoted by Model I and Model II. In Model I, we set  $h_1 = 0.1r$ ,  $h_2 = 0.5r$  and  $h_3 = 5r$  and whereas in Model II  $h_1 = 0.5r$ ,  $h_2 = r$  and  $h_3 = 5r$ . In both cases, the H I column densities of the stratified layers are chosen to be  $N_{HI} = 10^{21}$ ,  $10^{20}$  and  $10^{19} \text{ cm}^{-2}$ , respectively.

We obtain similar patterns in polarisation, which is weak near the H $\alpha$  centre and becomes strong in far wing regions. These polarisation patterns are also attributed to larger scattering numbers for photons near the line centre than those for far wing photons.

It is particularly notable that no flat profile near the line centre appears any longer. This is because of the contribution made by the small column density regions at high latitudes. These regions are optically thin for most of incident UV photons, and hence yields profiles proportional to the scattering cross section that is very steep near the line centre. In Model II shown in the right panel of Fig. 7, the profile is fairly extensive due to much larger column density than in the case of Model I shown in the left panel of the same figure.

### 3.4 Raman Scattering from the Receding Polar Components

In this subsection, we consider the Raman scattering from the receding polar scattering region of Component II whose existence is implied by Harries & Howarth (1996). In this work, we simply assume that this component is moving away from the emission source along the symmetry axis of the cylindrical shells considered in the previous subsections.

In the left panel of Fig. 8 we show the polarisation of H $\alpha$  wing photons Raman scattered in the receding polar region. We set the recession velocity of the polar component to be  $v_p = 100 \text{ km s}^{-1}$ . Since the symmetry axis and the scattering plane make a very small angle, the polarisation develops in the direction perpendicular to the symmetry axis, or in our formalism we obtain positive polarisation. For an observer in the equatorial direction, the scattering angle is nearly  $90^\circ$ , and therefore almost complete polarisation is obtained.

The wing flux is proportional to the scattering cross section and the incident UV flux in the optically thin limit. In the observer's rest frame, the scattering cross section peaks at the recessional velocity of the polar component  $v_p$ , and therefore we obtain the small peak at this velocity. Hence the resultant profile is obtained effectively by shifting the wing flux that is formed from Raman scattering in a static medium. Due to the incoherency of Raman scattering, the wing flux peaks at 6578 Å. This is interesting in that the symbiotic stars RR Tel and He 2-106 appear to exhibit a small and broad bump around 6580 Å just blueward of [N II] 6584 feature (Lee, Kang & Byun 2001).

In the right panel of Fig. 8, we present the Raman scattered wing fluxes obtained from combinations of a static cylindrical shell and a receding polar component. Since the two scattering components provide opposite senses of polarisation, the resultant polarisation is obtained by the algebraic sum of the two polarised flux components divided by the total flux. Therefore, in the blue wing, where the polar component contributes little, we obtain polarisation in the direction parallel to the symmetry axis. However, in the red wing, the polar component dominantly contributes to the final polarisation, yielding perpendicular polarisation.

## 4 DISCUSSION AND SUMMARY

We have investigated the polarisation of H $\alpha$  wings formed through Raman scattering of Ly $\beta$ . Two kinds of scattering regions are considered. The first one is a static cylindrical shell. From this component, the polarisation of H $\alpha$  wings develops in the direction parallel to the cylinder axis. It is particularly notable that stronger polarisation is obtained in far wing regions than near the line centre. Near the line centre, the scattering cross section is larger and therefore, Rayleigh scattering occurs more frequently than in far wing regions. The weaker polarisation in near wing regions is attributed to the larger Rayleigh scattering numbers than in far wing regions.

We consider the second scattering component that is located in the polar regions and moving away from the UV emission source with the recessional velocity  $v_p = 100 \text{ km s}^{-1}$ . The physical nature of this component is not certain, but the existence of this component is apparent from the spectropolarimetric observations presented by Harries & Howarth (1996). This component produces polarisation in the direction perpendicular to the symmetry axis. Since the scattering angle is almost  $90^\circ$ , nearly complete polarisation is obtained. Since the scattering component is moving away from the source, the wing flux peak appears at  $v = 6.4v_p$ , or around 6578 Å with our choice of  $v_p = 100 \text{ km s}^{-1}$ . Therefore, this polar component will produce a small bump in the wing profile which is strongly polarised in the direction perpendicular to the symmetry axis.

When the both scattering components coexist, we may observe the polarisation flip, where the blue part is characterised by parallel polarisation and the red part is polarised in the perpendicular direction. Therefore, if the scattering region is composed of a cylindrical shell subtends a fairly large solid angle with sufficient column density and a small receding polar component, the overall wing profile is determined by the cylinder component and the polarisation will be dominantly contributed by the polar component in the red part. Therefore in this case, we mainly obtain a profile that is nearly proportional to  $\Delta\lambda^{-2}$  and strongly polarised in the red part in the direction perpendicular to the symmetry axis.

This is very interesting considering the spectropolarimetric observation of the symbiotic star BI Crucis by Harries (1996), who reported the polarised H $\alpha$  wings in the direction perpendicular to the symmetry axis. He also noted that the polarisation is very strong in the red part. In his spectropolarimetric data, no polarisation flip is apparent. He interpreted his data using the assumption that the wings are formed through electron scattering. However, his data appear to be qualitatively consistent with the hypothesis that the H $\alpha$  wings are formed by Raman scattering in a fairly extensive cylindrical shell and a receding polar component.

Lee (1999) proposed that electron scattering of a monochromatic line radiation may leave polarisation structures. The radiative transfer process through Thomson scattering is diffusive both in real space and frequency space. This implies that photons that suffer more electron scattering tend to fall in both far and near wing regions, whereas those with fewer scattering numbers contribute to the formation of near wing regions. Since polarisation becomes weaker as the scattering number increases, we obtain weaker polarisation in the far wing regions in Thomson scattering media. Therefore, spectropolarimetry can be an important tool to investigate the wing formation mechanism.

Other factors that may affect the polarisation of Raman scattered H $\alpha$  wings and have not been considered in this work may include dust, kinematics of the cylindrical shell component. Currently, only few spectropolarimetric observations of H $\alpha$  wings can be found in the literature and little is known about the formation of H $\alpha$  profiles seen in symbiotic stars. We hope that more observation will provide constraints on various theoretical models of H $\alpha$  and other Balmer series line formation.

## ACKNOWLEDGMENTS

This work was supported by Korea Research Foundation Grant (KRF-2001-003-D00105).

## REFERENCES

- Arrieta A., Torres-Peimbert S., 2002, *Rev. Mex. Astron. Astrophys.* 12, 154
- Balick B., 1989, *AJ*, 97, 476
- Berestetskii V. B., Lifshitz E. M., Pitaevskii V. B., 1971, *Relativistic Quantum Theory*, Pergamon Press, Oxford
- Bernat A. P., Lambert D. L., 1978, *PASP*, 90, 520
- Bethe H. A., Salpeter E. E., 1957, *Quantum Mechanics of One and Two Electron Atoms*. Academic Press, New York
- Harries T. J., 1996, *A&A*, 315, 499
- Harries T. J., Howarth I. D., 1996, *A&AS*, 119, 61
- Ivison R. J., Bode M. F., Meaburn J., 1994, *A&AS*, 103, 201
- Karzas W. J., Latter R., 1961, *ApJS*, 6, 167
- Kenyon S. J., 1986, *The Symbiotic Stars*. Cambridge Univ. Press, Cambridge
- Lee H.-W., 1999, *ApJ*, 511, L13
- Lee H.-W., 2000, *ApJ*, 541, L25
- Lee H.-W., Blandford R. D., Western L., 1994, *MNRAS*, 267, 303
- Lee H.-W., Hyung S., 2000, *ApJ*, 530, L49
- Lee H.-W., Kang Y. W., Byun Y.-I., 2001, *ApJ*, 551, L121
- Lee H.-W., Lee K. W., 1997, *MNRAS*, 287, 211
- Lee H.-W., Park M.-G., 1999, *ApJ*, 515, 89
- Miranda L. F., Torrelles J. M., Eiroa C., 1996, *ApJ*, 461, L111
- Nussbaumer H., Schmid H. M., Vogel M., 1989, *A&A*, 211, L27
- Quiroga C., Mikolajewska J. Brandi E., Ferrer O., Garcia L., 2002, *A&A*, in press (astro-ph/0203288)
- Sadeghpour H. R., Dalgarno A., 1992, *J. Phys. B: At. Mol. Opt. Phys.*, 25, 4801
- Sakurai J. J., 1967, *Advanced Quantum Mechanics*, Addison-Wesley Publishing Company, MA.
- Saslow W. M., Mills D. L., 1969, *Phys. Rev.*, 187, 1025
- Schmid H. M., 1989, *A&A*, 211, L31
- Schmid H. M., 1996, *MNRAS*, 282, 511
- Selvelli P. L., Bonifacio P., 2000, *A&A*, 364, L1
- Schmutz W., Schild H., Mürset U., Schmid H. M., 1994, *A&A*, 288, 819

- Stenflo J. O., 1980, A&A, 84, 68  
van de Steene G. C., Wood P. R., van Hoof P. A. M., 2000, in ASP Conf. Ser. 199, Asymmetrical Planetary Nebulae II: From Origins to Microstructures, ed. J. H. Kastner, N. Soker, & S. Rappaport (San Francisco: ASP), 191  
van Groningen E., 1993, MNRAS, 264, 975  
van Winckel H., Duerbeck H. W., Schwarz H. E., 1993, A&AS, 102, 401

This paper has been typeset from a  $\text{\TeX}$ / $\text{\LaTeX}$  file prepared by the author.

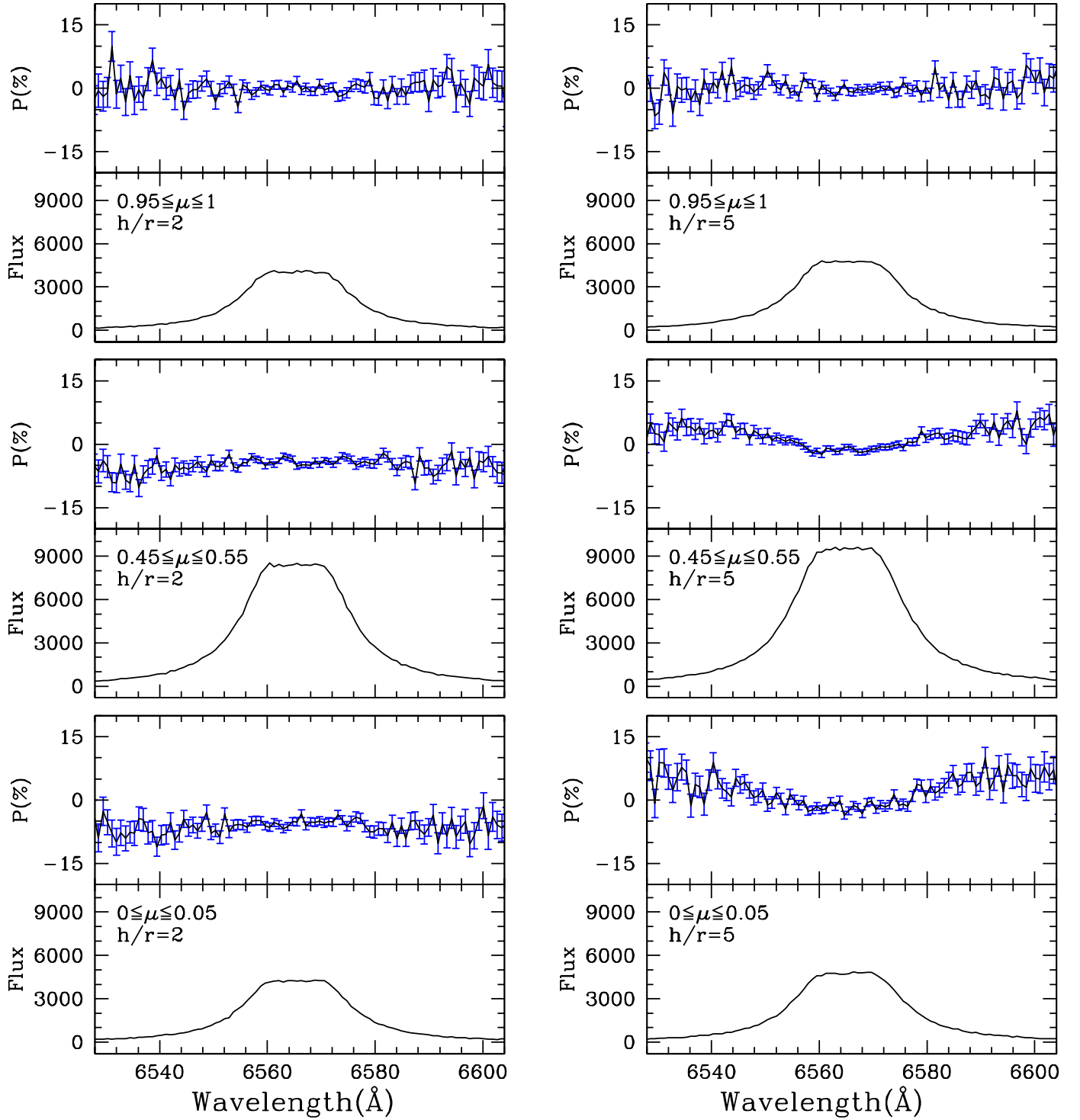


**Figure 6.** Profiles and polarisation of broad H $\alpha$  wings for various lines of sight. The height to radius ratios of the H I cylinder are 2 and 5 for left and right panels, respectively. Other parameters are the same as described in Fig. 5

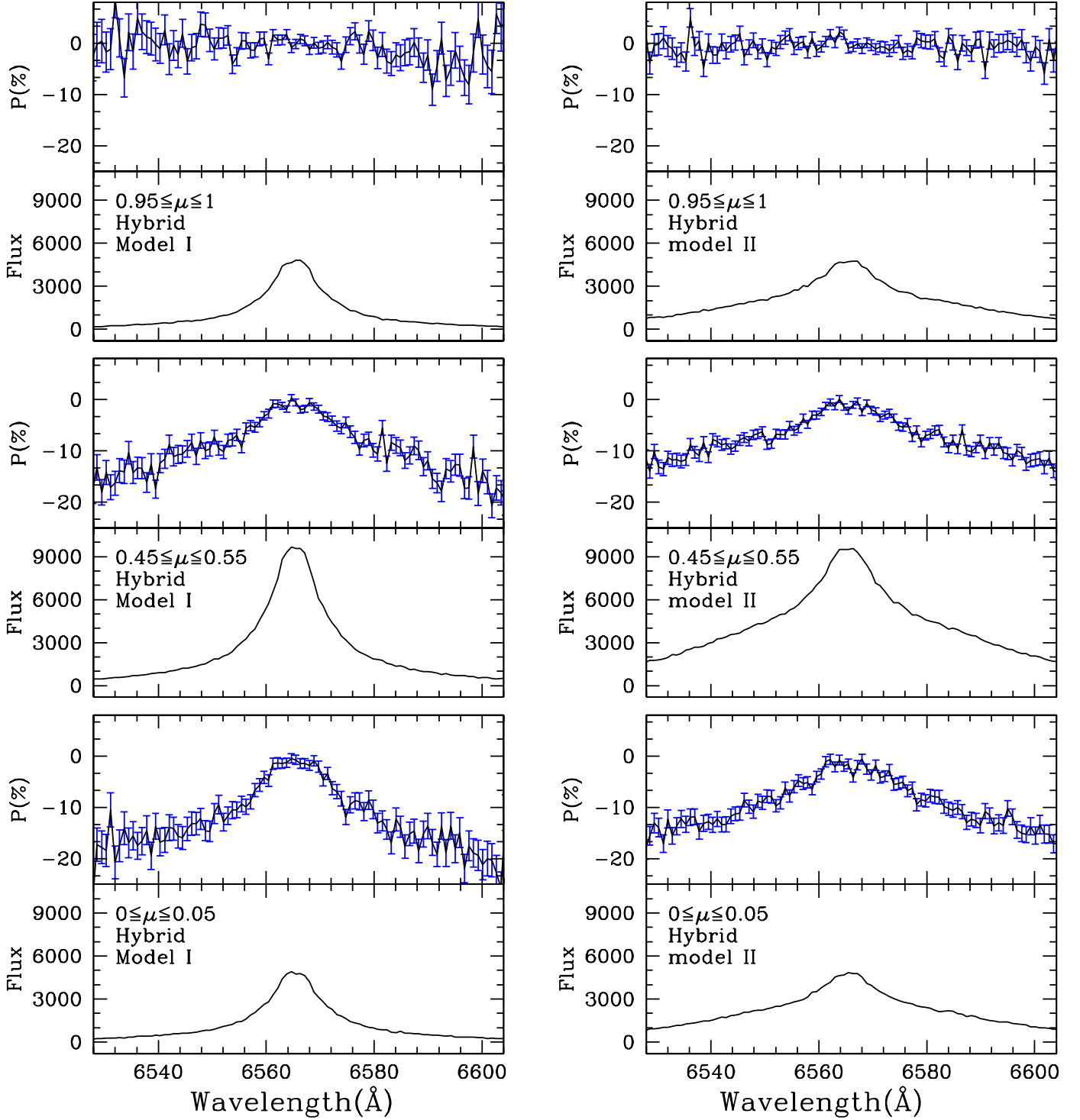


**Figure 7.** Profiles and polarisation of broad H $\alpha$  wings for the hybrid model. We consider only Component I in Fig. 2. The H I column densities are set to be  $10^{21}$ ,  $10^{20}$  and  $10^{19}$   $\text{cm}^{-2}$  from the equatorial region with  $h_1, h_2, h_3 = 0.1, 0.5$  and  $5$  in units of the radius  $r$  for the Hybrid Model I, and  $0.5, 1$  and  $5$  for the Hybrid Model II. Other parameters are the same as described in Fig. 5.

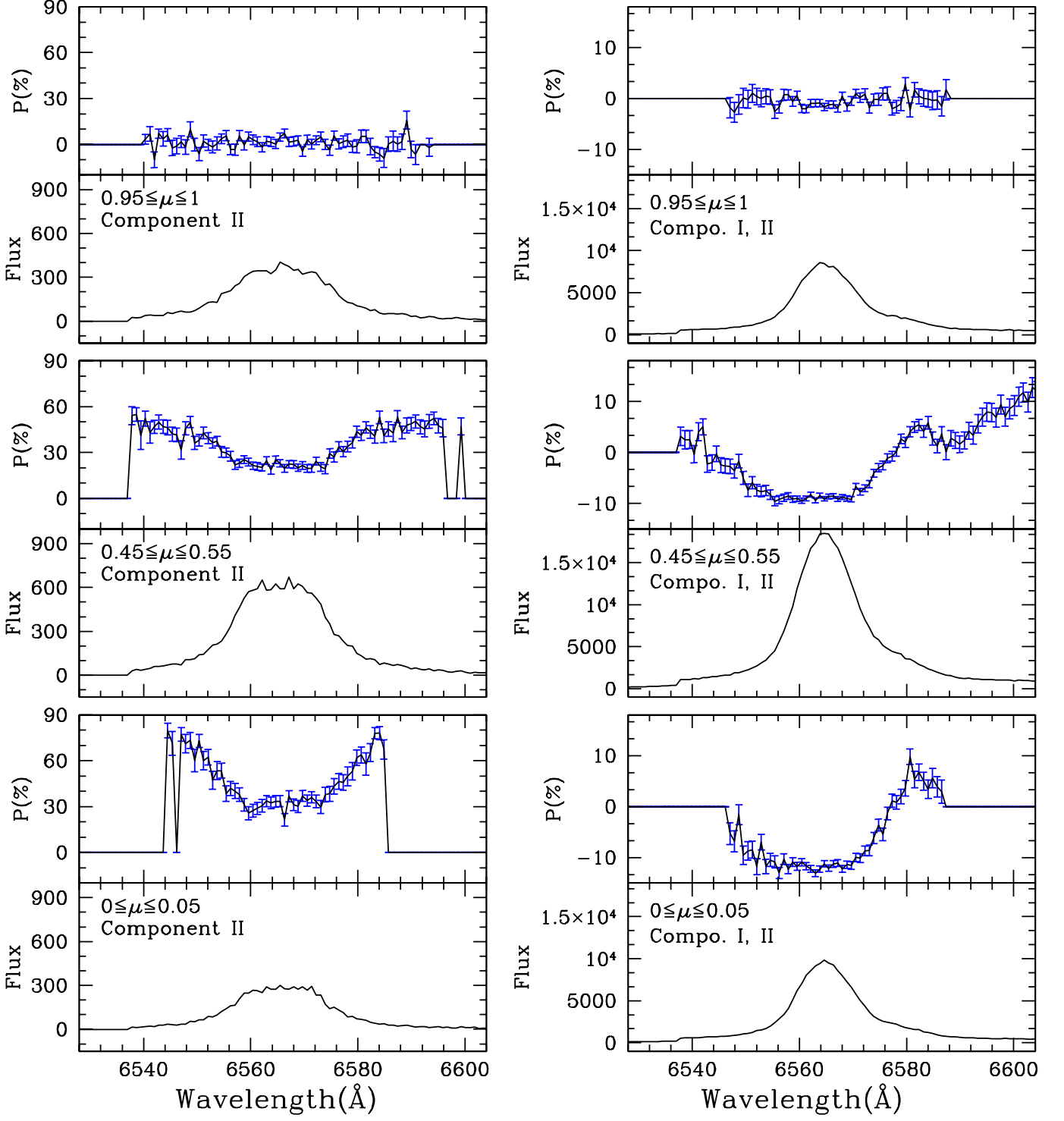


**Figure 8.** Profiles and polarisation of broad H $\alpha$  wings for both components. We set the recession velocity of the scattering region of Component II to be  $v_p = 100 \text{ km s}^{-1}$ , the half opening angle to be  $20^\circ$  and the ratio of Component I ( $h \equiv h_1 = h_2 = h_3$ ) to be  $h/r = 0.5$ .  $10^5$  UV photons in a bin with  $\Delta\lambda = 0.005 \text{ \AA}$  are injected to only Component II with H I column density  $10^{20} \text{ cm}^{-2}$  in the left panel, and to both components (H I column density  $10^{20}, 10^{23} \text{ cm}^{-2}$  for Component I and Component II, respectively) in the right panel. We omit denoting the polarisation when the photon flux is unnoticeably small. The error bars represent  $1-\sigma$ .